

Cite this: *J. Mater. Chem. A*, 2026, **14**, 7552

Zinc-induced ordering in L₁₀-type platinum-based nanoalloys for the electrocatalytic oxygen reduction reaction

Wu Tian,^a Ryota Sato,^b *^b Tomoki Uchiyama,^{†c} Yasutomi Tatetsu,^d Kenshi Matsumoto,^b Yoshiharu Uchimoto ^c and Toshiharu Teranishi *^{ab}

Platinum (Pt)-based intermetallic compound (IMC) nanoparticles (NPs) show high activity and durability in the oxygen reduction reaction (ORR) even in the highly acidic environment of polymer electrolyte fuel cells. Although Pt-based IMCs with L₁₀ crystal structure have been thoroughly studied, further improvement of ordering degree is required to enhance their ORR catalytic performance. Typical syntheses of L₁₀-ordered PtM (M is usually a 3d transition metal) IMC NPs require high-temperature annealing to induce the disorder–order transformation, which leads to unfavorable NP aggregation. Given that L₁₀-PtZn has a much lower phase transformation temperature than other L₁₀-PtM, Zn was included to allow the phase transformation of L₁₀-Pt(M,Zn) NPs to occur at relatively low temperature, thus suppressing aggregation and increasing the average ordering degree of NPs. We fabricated sub-6-nm L₁₀-Pt(M,Zn) NPs with a high ordering degree (>80%) through a facile wet chemical route followed by low-temperature annealing. Lattice constant tuning achieved by precise composition control revealed a positive correlation between the strain effect and corresponding ORR activity. Highly ordered L₁₀-Pt₅Co₄Zn₁ and L₁₀-Pt₅Ni₄Zn₁ NPs showed high specific activities of 1.71 and 1.40 mA cm_{Pt}⁻², respectively, which are almost comparable to that of L₁₀-PtCo NPs.

Received 10th October 2025
Accepted 13th January 2026

DOI: 10.1039/d5ta08256k

rsc.li/materials-a

1. Introduction

A proton-exchange membrane fuel cell (PEMFC) can be defined as a galvanic cell that converts chemical energy directly into electrical energy. PEMFCs show promise as a type of next-generation energy source because of their advantages including fast fueling, high energy density, and zero pollution.¹ However, the high cost, low efficiency, and short life time of the catalysts for the cathodic oxygen reduction reaction (ORR) are major technical obstacles for the production of commercially feasible PEMFCs. After decades of research developing highly efficient ORR catalysts, scarce and expensive platinum (Pt) is still an indispensable core component of cathodic ORR catalysts. Recent studies have shown that incorporation of transition metals (M) with smaller atomic radius (such as Fe, Co, Ni, Cu, *etc.*) into Pt nanoparticles (NPs) introduces beneficial

compressive strain into the Pt-rich atomic layers that are formed on the outermost surface by acid treatment. A theoretical study suggested that compressive surface strain in the Pt layer weakens its binding with oxygen intermediates, thus increasing the cathodic ORR performance of PtM-Pt core-shell (PtM@Pt) catalysts.² As highlighted by Pt₃Ni@Pt nanoframes,³ PtNi@Pt bunched nanocages,⁴ and Pt₃Co@Pt NPs,⁵ both alloying Pt with M, especially Co and Ni with quite small atomic radii, and constructing core-shell structures with Pt-rich surfaces can induce a compressive strain effect in the Pt outermost layer, which can effectively accelerate ORR kinetics as well as lower the Pt content of the catalysts. Although some catalysts achieved high ORR performance, most current Pt-based catalysts suffer from poor durability because of the leaching of M in the strongly acidic electrolyte at high potential, which leads to structural changes that decrease activity.

To prevent M leaching from PtM NPs, highly ordered PtM intermetallic compounds (IMCs) with well-defined stoichiometry have attracted much attention as stable core materials for surface strain-engineered PtM@Pt NPs recently. PtM IMCs possess higher acid corrosion resistance than that of disordered PtM NPs because of their larger formation enthalpy.^{6,7} There are already multiple reports on the synthesis of binary L₁₀-PtM and ternary L₁₀-type Pt (M₁,M₂) NPs as high-performance ORR catalysts including L₁₀-PtZn,⁸ L₁₀-PtNi,^{9,10} L₁₀-PtCo,^{6,11,12} L₁₀-PtFe,⁷ and L₁₀-PtCoNi.^{13,14} Low-temperature synthesis of Pt-

^aDepartment of Chemistry, Kyoto University, Uji, Kyoto 611-0011, Japan^bInstitute for Chemical Research, Kyoto University, Uji, Kyoto 611-0011, Japan. E-mail: r-sato@scl.kyoto-u.ac.jp; teranishi@scl.kyoto-u.ac.jp^cGraduate School of Human and Environmental Studies, Kyoto University, Sakyo-ku, Kyoto 606-8501, Japan^dDepartment of Health Informatics, Meio University, Biimata, Nago, Okinawa 905-8585, Japan[†] Present address: Department of Metallurgy, Materials Science and Materials Processing, Tohoku University, Sendai, Miyagi 980-8579, Japan.

based IMC NPs containing M with high melting points (Fe: 1535 °C; Co: 1495 °C; Ni: 1453 °C) is challenging even though Pt IMCs are thermodynamically more favourable than their solid-solution counterparts at room temperature.¹⁵ High-temperature thermal annealing is usually required to induce phase transformation from disordered PtM alloys into ordered PtM IMCs in the solid state by overcoming the high energy barrier for atom diffusion to achieve ordering.^{16,17} High-temperature annealing causes severe sintering of NPs, especially when at high NP loading on supports, resulting in a large decrease of the specific surface area (surface-to-volume ratio) of the NPs. In addition, the long-range order parameter (S) that quantifies the ordering degree is compromised when the annealing temperature exceeds the relatively lower phase-transition temperature (T_{PT}) from an $L1_0$ -type IMC to A1-type solid solution in the corresponding bulk Pt–M binary phase diagram (T_{PT} : PtFe \sim 1300 °C, PtCo \sim 820 °C, PtNi \sim 630 °C).⁹ For NPs with high specific surface area, T_{PT} decreases because of the increased contribution of entropy as a function of temperature in the Gibbs free energy equation resulting from the increased exposure of the disordered surface. Thus, as a problem unique to NPs with a size distribution, a situation may arise where smaller particles with A1 structure and particles with $L1_0$ structure that are larger than a critical particle size coexist depending on the heat treatment temperature. As a result, the average S for ensemble NPs tends to decrease with particle size. The S achieved after thermal annealing, which is the key parameter to improve the electrocatalytic performance of $L1_0$ -PtM, has seldom been discussed in previous studies. A feasible way to improve the ordering degree of small IMC NPs and thus increase the activity and durability of ORR catalysts for fuel-cell applications still needs to be demonstrated.

The introduction of low-melting-point metals into IMC nanoparticles (NPs) is a promising strategy for lowering the activation energy of atomic diffusion.^{16–18} Elements from groups 12–15 are suitable candidates due to their low melting points, such as Zn (420 °C), Cd (321 °C), Ga (30 °C), In (157 °C), Sn (232 °C), Pb (328 °C), and Bi (\sim 271 °C). However, incorporating such metals may reduce the compressive strain in the surface Pt atomic layers, thereby decreasing the specific activity for the oxygen reduction reaction (ORR), because most of these metals have larger atomic radii than 3d transition metals such as Co and Ni (atomic radius: Co \sim 125 pm, Ni \sim 125 pm). Among these low-melting-point metals, we selected Zn because it has a relatively small atomic radius (134 pm) and forms a thermodynamically stable $L1_0$ structure with Pt.

Herein, we use an organometallic zero-valence Zn complex to incorporate hard-to-reduce Zn into Pt–M NPs by a facile wet method. The incorporation of Zn lowers the ordering temperature of Pt–M–Zn NPs in the formation of ordered IMC NPs, which suppresses sintering and leads to a high ordering degree. To improve ORR activity, *i.e.*, to optimize the strain effect on the Pt outermost layer formed by acid treatment, compositionally controlled $L1_0$ -type Pt(M,Zn) (M = Co or Ni) NPs with high ordering degree are synthesized through low-temperature annealing. The activity of the highly ordered $L1_0$ -Pt₅Co₄Zn₁

and $L1_0$ -Pt₅Ni₄Zn₁ NP catalysts is investigated under ORR conditions relevant to PEMFCs.

2. Experimental

2.1 Chemicals

Platinum(II) acetylacetonate (Pt(acac)₂, 97%), cobalt(III) acetylacetonate (Co(acac)₃, 98%), nickel(II) acetylacetonate (Ni(acac)₂, 95%), oleylamine (OAm, 80–90%), borane-*tert*-butylamine complex (BBA, 97%), and Nafion (5% in a mixture of 2-propanol and water) were purchased from Sigma-Aldrich. Diphenylzinc (Ph₂Zn, 99%), *n*-hexane (98.5%), and ethanol (>99%) were purchased from Fujifilm Wako Pure Chemical. Ph₂Zn was dissolved in OAm to form a 10 mM solution and stored in an argon (Ar)-filled glovebox. Other chemicals were used without further purification.

2.2 Synthesis of A1-type Pt–M–Zn (M = Co, Ni) NPs

As a typical synthesis of A1-type Pt₅Co₄Zn₁ NPs, 0.05 mmol of Pt(acac)₂, 0.048 mmol of Co(acac)₃, 1.6 mL of 10 mM Ph₂Zn OAm solution, and 5.0 mL of OAm were mixed in a glass pressure tube in a glovebox under an inert reaction atmosphere. The reaction solution was heated with an oil bath at 80 °C for 30 min and then at 230 °C for 120 min, followed by cooling to room temperature. Next, 10 mL of *n*-hexane and 30 mL of ethanol were added to the reaction solution to precipitate the product. After centrifugation at 9000 rpm (9510 rcf) for 15 min and washing three times with a 1 : 4 volume ratio mixture of *n*-hexane and ethanol, A1-type Pt₅Co₄Zn₁ NPs were collected and dispersed in *n*-hexane for further use. By adjusting the feed ratio of Co(acac)₃, Ni(acac)₂, and Ph₂Zn, the compositions of A1-type Pt–M–Zn NPs were changed as desired. For the preparation of Pt₅Ni₅ NPs, 10 mg of BBA was added as a stronger reductant to decrease the NP size.¹⁹

2.3 Preparation of carbon-supported $L1_0$ -Pt(M,Zn)@Pt NPs ($L1_0$ -Pt(M,Zn)@Pt/C)

Carbon black (60 mg, Vulcan XC-72) was suspended in 60 mL *n*-hexane by sonication for 30 min and then an *n*-hexane dispersion of A1-type Pt–M–Zn NPs was added to this suspension. The loading amount of Pt was maintained at around 11 to 14 wt%. After sonication for 1 h, the carbon-supported Pt–M–Zn NPs (Pt–M–Zn/C) were dried and annealed under 4% hydrogen (H₂) in Ar at a designated temperature (550 or 600 °C) to convert the A1 structure into $L1_0$ structure. $L1_0$ -Pt(M,Zn)/C was then treated in 0.1 M HClO₄ aqueous solution at 60 °C for 12 h to give carbon-supported catalysts with $L1_0$ -Pt(M,Zn)-Pt core-shell NPs ($L1_0$ -Pt(M,Zn)@Pt/C) for further study. Disordered A1-PtCo@Pt/C and A1-PtNi@Pt/C catalysts for ORR testing were synthesized using identical procedures, followed by annealing at 400 °C to ensure uniform elemental distribution.

2.4 Thermogravimetric analysis (TGA) to measure Pt loading amount

TGA was conducted to measure the Pt loading amount of $L1_0$ -Pt(M,Zn)@Pt/C. Before sample measurement, a blank TGA



measurement was conducted using an empty pan under the same conditions as the sample measurement for background correction. The sample measurement was then conducted under 20% oxygen (O₂) in nitrogen (N₂) flowing at 300 mL min⁻¹. Temperature programming was set at 5 °C min⁻¹ from 50 to 1000 °C to fully oxidize the carbon support. The residue consisted of Pt alloys. Background correction was performed by subtracting the thermogravimetric curve of the blank measurement from that of the sample. The Pt mass loading of each sample was determined by combining TGA results with the sample composition determined by scanning electron microscopy-energy-dispersive X-ray spectroscopy (SEM-EDX).

2.5 Estimation of surface strain in L1₀-Pt(M,Zn)@Pt NPs

The surface strain in the Pt shell on the L1₀-Pt(M,Zn) core of the L1₀-Pt(M,Zn)@Pt NPs was estimated by comparison of the area of a triangle consisting of three neighboring atoms on {111} planes of L1₀-Pt(M,Zn) and that of pure Pt using the following equation to calculate the lattice mismatch strain.

$$\text{Strain}(\%) = \frac{S - S_{\text{Pt}}}{S_{\text{Pt}}} \quad (1)$$

where S and S_{Pt} represent the triangle areas of L1₀-Pt-M-Zn and pure Pt, respectively, as indicated in Fig. S2. S and S_{Pt} were calculated from the lattice constant obtained by Rietveld refinement of the powder X-ray diffraction (XRD) pattern of L1₀-Pt-M-Zn and the literature value for the lattice constant of Pt (see Table S1), respectively.¹⁰ A negative value of strain corresponds to compressive strain in the Pt shell.

2.6 Calculation of the long-range order parameter of L1₀-Pt(M,Zn) NPs

The average degree of chemical (atomic) order for ensemble L1₀-Pt(M,Zn) NPs can be evaluated as the long-range order (LRO) parameter (S) extracted from the XRD pattern by comparing the integrated intensity ratio of the 110 superlattice reflection peak to the principal 111 reflection peak, I_{110}/I_{111} . The experimental I_{110}/I_{111} derived from the refined XRD pattern can be defined as:²⁰

$$I_{110}/I_{111} = S^2(I_{110}^*/I_{111}^*) \quad (2)$$

where S is the LRO parameter and I_{110}^*/I_{111}^* is the simulated intensity ratio for the perfectly ordered L1₀-type intermetallic compound (IMC) with the ideal stoichiometric compositions of Pt₅₀M_{50-x}Zn_x. Thus, S values for perfectly ordered L1₀-Pt(M,Zn) and perfectly disordered A1-Pt(M,Zn) alloys are 1 and 0, respectively. To experimentally determine I_{110} and I_{111} with a high degree of accuracy, Rietveld refinement was performed in the 2θ range of 30° to 90° to avoid interference from the broad peak around 25° derived from the carbon support. The I_{110}^*/I_{111}^* ratio depends on the composition of Pt₅₀M_{50-x}Zn_x to a non-negligible degree. Therefore, the I_{110}^*/I_{111}^* ratios of fully ordered alloys with corresponding compositions were simulated, as listed in Table S2.

2.7 Catalyst ink preparation and electrochemical measurements

Catalyst ink for electrochemical measurements was prepared by mixing carbon-supported catalyst (1 mg) with ultrapure water (800 μL), 2-propanol (200 μL), and Nafion solution (5 wt%, 10 μL) and sonicating the mixture for 1 h. Catalyst ink (10 μL) was then deposited on a glassy carbon rotating disk electrode (5 mm in diameter) and dried *via* a spin-assisted method at 700 rpm. The experiments were conducted in 0.1 M HClO₄ electrolyte using a three-electrode system with Pt wire as a counter electrode and a reversible hydrogen electrode (RHE, 5% H₂) as a reference electrode. The measured potential was corrected by adding 0.0385 V according to the Nernst equation. Cyclic voltammetry (CV) and linear sweep voltammetry (LSV) were used to evaluate catalytic performance. All potentials are referenced to RHE. Cleaning CV measurements were conducted by scanning the electrode in the range of 0.02–1.20 V at 100 mV s⁻¹ for 50 cycles under N₂ saturation. The final CV was collected in the range of 0.02–1.10 V at 50 mV s⁻¹ to calculate the electrochemical surface area (ECSA) from the H_{upd} adsorption peak area of the final CV. LSV of the ORR was conducted by positively scanning from 0.2 to 1.2 V at 10 mV s⁻¹ during rotation at 2500 to 100 rpm in an O₂-saturated atmosphere. The final ORR linear scanning current was corrected by subtracting the current obtained in N₂-saturated atmosphere using the same method and conditions. The specific activity (i_s) and mass activity (i_m) at 0.9 V (vs. RHE) were calculated based on the Koutecky–Levich equation. Accelerated durability tests (ADTs) were conducted in a half-cell configuration using constant-potential polarization at 0.60 and 0.95 V (3 s at each potential). After every 2500 cycles, cyclic voltammograms (CVs) were recorded to evaluate the ECSA of the catalysts.

2.8 Material characterization

The SEM-EDX measurements were performed using an Edax Apollo XF attachment on a scanning electron microscope (SEM, Hitachi S-4800) at 20 kV, which detected Co-K, Ni-K, Zn-K, and Pt-L peaks. XRD patterns were collected at room temperature using a powder diffractometer in Bragg–Brentano configuration (Malvern Panalytical Aeris) with Cu K α radiation ($\lambda = 1.542 \text{ \AA}$) at 40 kV and 15 mA. Rietveld refinements were performed using HighScore Plus, which is the commercial powder diffraction analysis software from Malvern Panalytical.²¹ Magnetic hysteresis M–H loops were measured on a superconducting quantum interface device (Quantum Design MPMS3) with a field of up to 7 T. Transmission electron microscopy (TEM) images were obtained on a transmission electron microscope (HT7820, Hitachi) at an accelerating voltage of 120 kV. High-resolution transmission electron microscopy (HRTEM), high-angle annular dark field-scanning transmission electron microscopy (HAADF-STEM), EDX spectroscopy, and electron energy loss spectroscopy (EELS) were conducted with a transmission electron microscope (JEM-ARM200F, JEOL) at an accelerating voltage of 200 kV.



2.9 Computational calculations

Density functional theory (DFT) calculations were performed on L_{10} -Pt $_1$ M $_1$ (M = Fe, Co, Ni, Zn) and Zn-doped L_{10} -Pt $_1$ M $_{0.5}$ Zn $_{0.5}$ (M = Fe, Co, Ni) systems using the OpenMX code.²² The generalized gradient approximation of Perdew–Burke–Ernzerhof was employed for the exchange–correlation functional, and pseudo-atomic orbital basis sets (s3p2d1 for Fe, Co, Ni, and s3p2d2f1 for Pt) were used. Cutoff radii were set to 6.0 a.u. for Fe, Co, Ni, and 9.0 a.u. for Pt, with a cutoff energy of 500 Ry. A k -point mesh of $23 \times 23 \times 17$ was used for Zn-doped L_{10} -Pt $_1$ M $_{0.5}$ Zn $_{0.5}$ systems and one of $16 \times 16 \times 17$ was used for the other systems. Conventional cells were chosen as $1 \times 1 \times 1$ for L_{10} -Pt $_1$ M $_1$ systems and $\sqrt{2} \times \sqrt{2} \times 1$ for Zn-doped L_{10} -Pt $_1$ M $_{0.5}$ Zn $_{0.5}$ systems to accommodate for different atomic positions. The formation energies E_{form} of L_{10} -Pt $_1$ M $_1$ and L_{10} -Pt $_2$ M $_1$ Zn $_1$ were calculated using the following equation.

$$E_{\text{form}} = E_{\text{alloy}} - (\alpha \times \mu[\text{Pt}] + \beta \times \mu[\text{M}]) \quad (3)$$

where E_{alloy} is the total energy of the alloys; $\mu[\text{Pt}]$ and $\mu[\text{M}]$ are the chemical potentials of Pt and M, respectively, which are equivalent to the total energies of these ground states; and α and β are integers.

To investigate the effects of Zn addition on L_{10} -PtM (M = Fe, Co, Ni) and its structural stability, E_{form} calculations were performed for systems where Zn was added to L_{10} -PtM and A1-PtM. The generation of structures with different Zn concentrations was accomplished using special quasirandom structures (SQS), which can consider randomness with high accuracy.²³ The generated structures were constructed using a $2 \times 2 \times 2$ supercell of the L_{10} structure, which contained a total of 32 atoms: 16 Pt atoms and either M or Zn atoms (16 in total). In the A1 structure, the randomness of all elements was considered, whereas in the L_{10} structure, only the positions of the Pt atoms were fixed, allowing for substitutions of M atoms and Zn. For each Zn concentration x , all structures generated by SQS were selected, with a constant Pt concentration. E_{form} calculations were conducted using Matlantis v.7.0.0, a versatile atomistic simulator that implements neural network potentials.²⁴ By performing structural optimizations on all model structures generated by SQS, the total energy of the systems was obtained. Subsequently, E_{form} for each system was calculated.

3. Results and discussion

3.1 Synthesis of highly ordered alloy L_{10} -Pt(M,Zn)@Pt/C

Considering that L_{10} -PtZn possesses a much lower T_{PT} than those of other L_{10} -PtM alloy NPs, we envisioned that Zn would promote ordering in the transformation of A1 to L_{10} structure at relatively low temperature to achieve both a high degree of ordering and sintering suppression. However, incorporation of hard-to-reduce Zn into nanosized PtM alloy with ideal composition and monodispersity is challenging because of the large negative standard electrode potential of Zn^{2+}/Zn (E° at 25 °C = -0.76 V). Synthesis of PtZn IMC NPs usually involves the reduction of Zn^{2+} in Pt/ Zn^{2+} nanocomposites, such as Pt NPs encapsulated in a ZnO matrix,⁸ Pt NPs surrounded by zeolitic

imidazolate frameworks containing Zn^{2+} ,¹⁸ Pt NPs coated with a thin ZnO shell,²⁵ and Zn-covered Pt NPs obtained by Zn vapor deposition.²⁶ The high reaction temperature and complicated procedures in these strategies make it difficult to properly manipulate the composition and morphology of PtZn IMC NPs.

Here, we used an organometallic zero-valence Zn complex to incorporate difficult-to-reduce Zn into Pt–M NPs by a facile wet chemical process to synthesize monodisperse Pt–M–Zn NPs. Zero-valent organozinc enables mild and well-controlled incorporation of Zn, suppressing independent Zn nucleation and promoting homogeneous alloying, which leads to uniform nanoparticle morphology and composition. The overall synthesis of carbon-supported L_{10} -type Pt(M,Zn)-Pt core-shell NPs (denoted as L_{10} -Pt(M,Zn)@Pt/C) is schematically represented in Fig. 1. First, platinum(II) bis(acetylacetonate) (Pt(acac)₂), cobalt(III) tris(acetylacetonate) (Co(acac)₃), nickel(II) bis(acetylacetonate) (Ni(acac)₂), diphenylzinc (Ph₂Zn) with specified molar ratios were co-reduced in oleylamine (OAm). Ph₂Zn with zero-valence state Zn was used to directly incorporate Zn into the PtM alloys to avoid the Zn^{2+} reduction procedure. The synthesized A1-type (*i.e.*, face-centered cubic (fcc)-based solid solution) Pt–M–Zn NPs were supported on carbon (denoted as A1-Pt–M–Zn/C) and then transformed into highly ordered L_{10} structure by low-temperature reductive annealing (denoted as L_{10} -Pt(M,Zn)/C), followed by acid post-treatment to generate a Pt shell on the NP surface (L_{10} -Pt(M,Zn)@Pt/C).

3.2 Precise composition control and phase transformation of A1-Pt–M–Zn NPs

Fig. 2A–F and S4A, B show transmission electron microscopy (TEM) images of the as-synthesized Pt–M–Zn NPs and corresponding size distributions. The average sizes of the monodisperse Pt–M–Zn NPs determined by measuring 200 randomly selected NPs for each sample were 3.5–6.5 nm, which matched well with X-ray diffraction (XRD) results (Table S3). The particle size decreased with increasing Zn content in both M cases because of highly active Ph₂Zn.²⁷ Based on the theory that too large or too small particle size is not suitable in terms of electrochemically active surface area (ECSA) or ordering from A1 to L_{10} structure during annealing, respectively, the optimal NP size is empirically considered to be in the 4–6-nm range. For the specific stoichiometry required for L_{10} structure formation, we

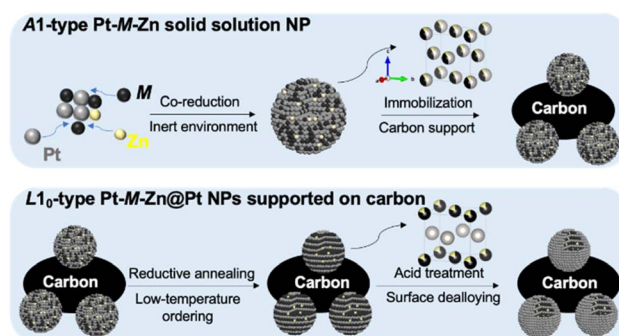


Fig. 1 Synthesis of L_{10} -type Pt(M,Zn)@Pt NPs supported on carbon.



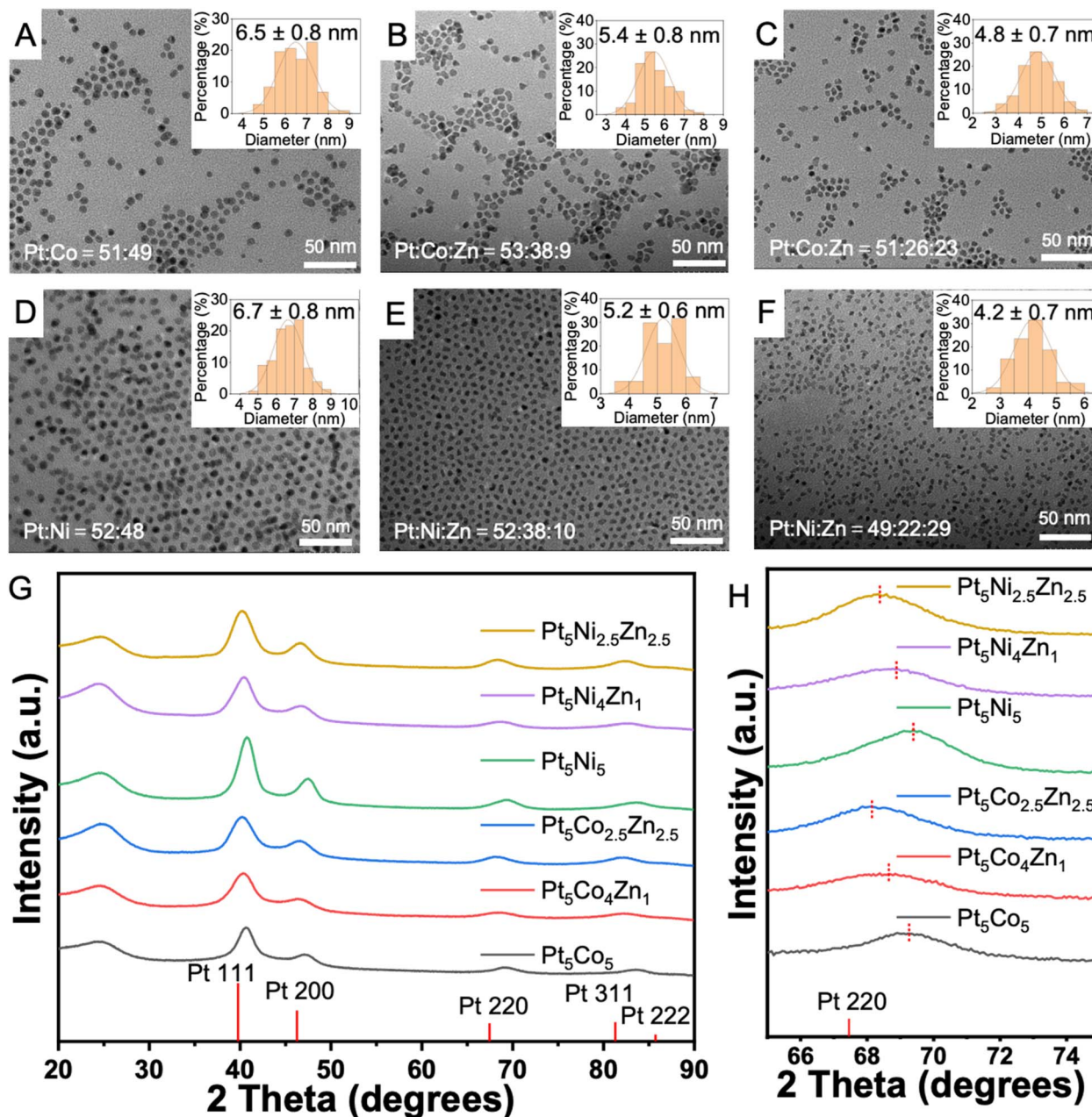


Fig. 2 Characterization of A1-Pt(M,Zn)/C NPs. TEM images, elemental compositions (at%), and size distributions (inset) of as-synthesized (A) A1-Co₅Pt₅, (B) A1-Pt₅Co₄Zn₁, (C) A1-Pt₅Co_{2.5}Zn_{2.5}, (D) A1-Ni₅Pt₅, (E) A1-Pt₅Ni₄Zn₁, and (F) A1-Pt₅Ni_{2.5}Zn_{2.5} NPs. (G and H) XRD patterns of A1-Pt(M,Zn)/C before reductive annealing. The broad peak at around 25° was ascribed to the carbon support.

controlled the atomic ratio of Pt/nonprecious metal in the NPs to be around 1 : 1 (Table S4). The XRD patterns of a series of as-synthesized Pt-M-Zn/C are presented in Fig. 2G and H. The diffraction peaks indicate that their crystal structures are fcc, meaning that the Pt-M-Zn NPs possess A1 structure with disordered distributions of all elements. The diffraction peaks shift to lower angle with increasing Zn/M ratio.

The as-synthesized A1-type NPs uniformly distributed on carbon supports were subjected to reductive annealing to induce phase transformation. The loading amount of Pt was controlled in the range of 11–15 wt%, as confirmed by

thermogravimetric analysis (see Table S4). Although ordering of PtM NPs at high temperature is usually accompanied by sintering,²⁸ severe sintering was not observed for A1-Pt-M-Zn/C annealed at 600 and 550 °C (see Fig. S5 and S6, respectively). XRD patterns of annealed samples (Fig. 3A, B, D and E) contained symmetric and broad diffraction peaks, indicating no severe aggregation, and new clear superlattice peaks at 33° (assignable to 110 peaks) demonstrating the formation of the L₁ structure. As expected from calculations, we observed splitting of the 200 peaks of fcc structure into 200 and 002 peaks of L₁ structure with shifts of the 200 peak to lower angle and



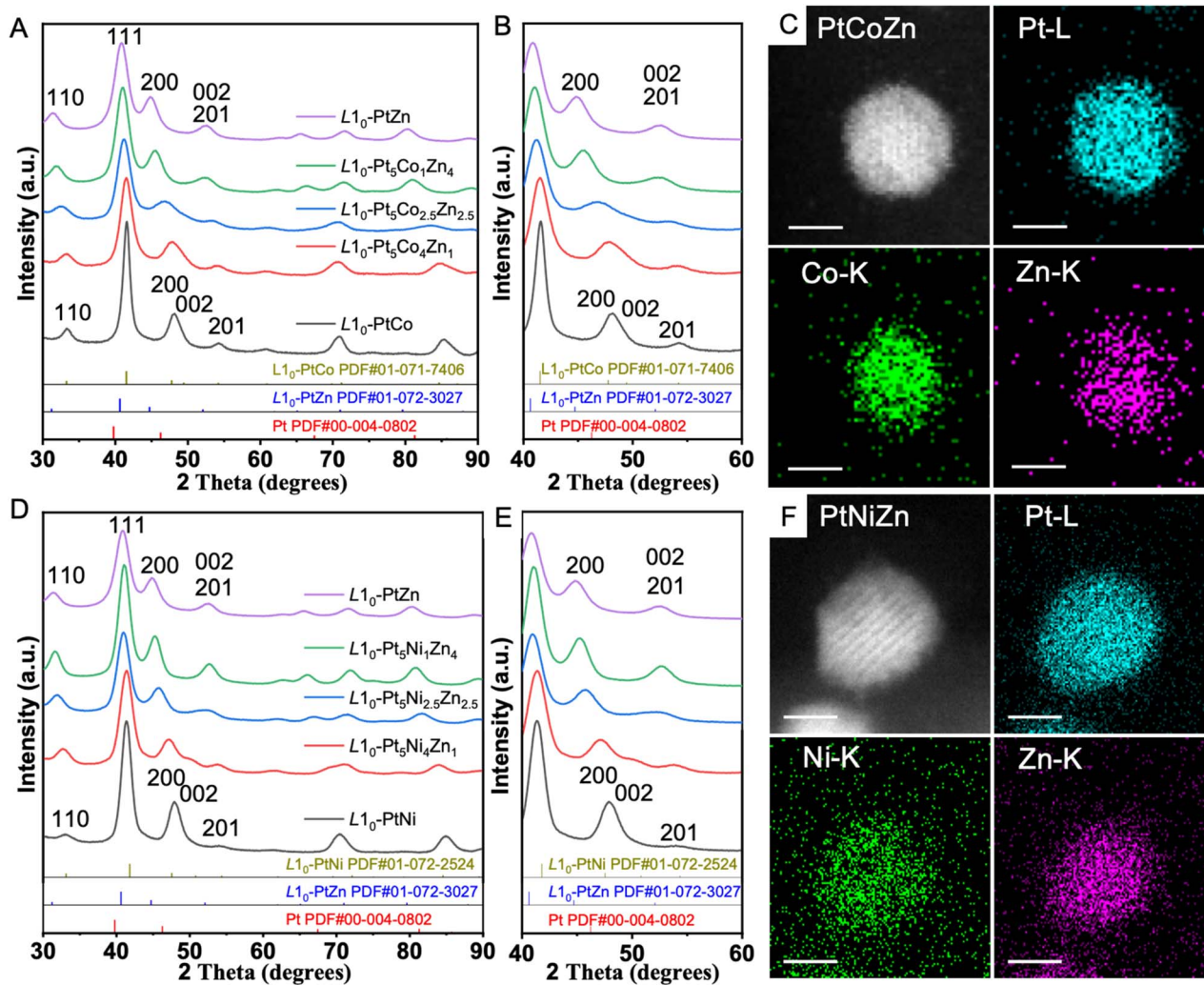


Fig. 3 Characterization of L_{10} -Pt(M,Zn)/C NPs. (A and B) XRD patterns of L_{10} -Pt(Co,Zn)/C. (C) STEM image and corresponding elemental mapping images of a single L_{10} -Pt₅Co_{2.5}Zn_{2.5} NP. (D and E) XRD patterns of L_{10} -Pt(Ni,Zn)/C NPs. (F) STEM image and corresponding elemental mapping images of a single L_{10} -Pt₅Ni_{2.5}Zn_{2.5} NP (Pt: blue, Co or Ni: green, Zn: purple).

002 peak to higher angle with increasing Zn content. These changes indicated longer lattice constants along $\langle 100 \rangle$ directions (a and b) and shorter lattice constants along $\langle 001 \rangle$ directions (c) after annealing; that is, tetragonality (a/c) increased, consistent with the formation of L_{10} structure. Element distributions in L_{10} -Pt(Co,Zn) and L_{10} -Pt(Ni,Zn) were further analyzed by high-angle annular dark field scanning transmission electron microscopy (HAADF-STEM) and energy-dispersive X-ray spectroscopy (EDS) mapping. Uniform distributions of three elements in individual NPs were observed for both L_{10} -Pt(Co,Zn) and L_{10} -Pt(Ni,Zn) NPs, indicating no phase segregation after reductive annealing with or without subsequent acid treatment (Fig. 3C, F and S7–S11). These results strongly confirmed that the disordered A1 structure of the as-synthesized NPs with various Zn/M ratios was converted to ordered L_{10} structure by reductive annealing.

3.3 Zn-promoted formation of highly ordered L_{10} -Pt(M,Zn) NPs

S is a critical parameter that determines both the activity and durability of catalysts. S of the NPs was evaluated by calculating the integrated intensity ratio I_{110}/I_{111} obtained from the Rietveld refinement of XRD data (see Fig. S12 and S13 and Methods in the SI).^{29,30} L_{10} -Pt₅Co₅/C and L_{10} -Pt₅Ni₅/C obtained by reductive annealing for 6 h at 600 and 550 °C, respectively, showed S of 65% and 47%, respectively. L_{10} -Pt₅Co₄Zn₁/C and L_{10} -Pt₅Ni₄Zn₁/C obtained under the same conditions possessed higher S of 78% and 81%, respectively, which was induced by the small amount of Zn. When the annealing temperature of A1-Pt₅Co₅/C was increased from 600 to 650 °C, S of the resulting L_{10} -Pt₅Co₅/C reached 79%, although obvious sintering took place in areas with high NP density (Fig. S14). Different from L_{10} -Pt₅Co₅/C, S of L_{10} -Pt₅Ni₅/C obtained by annealing A1-Pt₅Ni₅/C at 600 °C was 36%, probably because of the low T_{pr} of PtNi of ~630 °C (Fig. S15). These results demonstrate that the initiation of



ordering at lower relative temperature in the presence of Zn is effective for obtaining highly ordered L1₀-Pt(M,Zn)/C. The *S* values of L1₀-Pt(Co,Zn)/C and L1₀-Pt(Ni,Zn)/C obtained at various annealing temperatures are summarized in Table S5. These values clearly show that *S* was increased by the presence of Zn even for small NPs. To study the effect of NP size on *S* without Zn incorporation, L1₀-Pt₅Co₅/C and L1₀-Pt₅Ni₅/C with a size of around 5 nm were also synthesized. These samples exhibited lower *S* than their larger counterparts (Fig. S16, S17 and Table S5). These results further emphasize the importance of Zn incorporation for achieving high *S* in small NPs.

To consider the origin of the increase of *S* achieved by the addition of Zn, the formation energies (E_{form}) of A1- and L1₀-Pt(M,Zn) with various compositions were estimated by theoretical calculations. Calculated E_{form} of binary PtM at 0 K are more negative in the order PtCo < PtNi < PtFe < PtZn for both A1 and L1₀ structures (Fig. S18 and S19). The L1₀ structure is the thermodynamically stable phase with larger E_{form} than the A1 structure for all PtM in the low temperature region. The difference between E_{form} of the A1 and L1₀ structures ($\Delta E_{\text{form}} = E_{\text{form}}[\text{A1}] - E_{\text{form}}[\text{L1}_0]$) of each PtM is shown in Fig. S19B. ΔE_{form} is an indicator of the difficulty of phase transformation from L1₀ to A1 at high temperature. A larger positive value of ΔE_{form} indicates that the phase transformation can occur at higher temperature. ΔE_{form} increased in the order PtNi < PtCo < PtFe < PtZn, corresponding to the ascending order of T_{PT} obtained from bulk Pt–M binary phase diagrams (T_{PT} : PtNi ~630 °C < PtCo ~820 °C < PtFe ~1300 °C, PtZn over 900 °C [data over 900 °C are not available]). ΔE_{form} of Pt₁M_{1-x}Zn_x with various compositions (0 < *x* < 1) are summarized in Fig. S19. The tendency of ΔE_{form} to increase with Zn content in all systems strongly suggests that the incorporation of Zn contributes to the increase of T_{PT} by making the L1₀ structure more stable than the A1 structure with the same composition, resulting in the promotion of L1₀ ordering even for small NPs.

The high degree of ordering induced by the introduction of Zn was further confirmed by magnetic measurements, as shown in Fig. S20. L1₀-Pt₅Co₅, Pt₅Co₄Zn₁, and Pt₅Co_{2.5}Zn_{2.5} obtained by reductive annealing at 600 °C for 6 h exhibited superparamagnetic behavior at 27 °C and almost no coercivity (H_c), which could be explained by the low blocking temperature caused by their small NP size.³¹ Magnetic hysteresis loops were then measured at –263 °C. L1₀-Pt₅Co₅ showed hard magnetic properties with low H_c (2.6 kOe) and high saturation magnetization. In contrast, both L1₀-Pt₅Co₄Zn₁ and L1₀-Pt₅Co_{2.5}Zn_{2.5} exhibited harder magnetic properties with higher H_c of 10.0 and 12.0 kOe, respectively, and lower saturation magnetization.³² This change in magnetic properties induced by Zn substitution could be explained by the increase in H_c caused by the increase in magnetic anisotropy resulting from the increase in the tetragonality of the L1₀ structure (see Table S5) and the decrease in magnetization caused by the decreased content of 3d lone-pair electrons. The approximately single-phase loops of L1₀-Pt₅Co₄Zn₁ and L1₀-Pt₅Co_{2.5}Zn_{2.5} also indicate the uniform distribution of Zn atoms at an atomic level in the NPs. These results confirmed that Zn incorporation promoted atom

diffusion at lower temperature, resulting in the formation of L1₀ structures with high *S*.³³

3.4 Formation of compressed Pt-rich shells on L1₀-Pt(M,Zn) cores

To use the series of L1₀-Pt(M,Zn)/C as ORR catalysts, the samples were first subjected to acid treatment to generate Pt-rich shells through the etching of M from the NP surface. Elemental compositions before and after acid treatment were analyzed by SEM-EDX, from which it was confirmed that around 50% of M remained in the ordered L1₀ NPs (Table S4). Contrary to the ordered L1₀ NPs, dramatic decreases of M content were observed in disordered A1-PtM NPs (PtNi: 48% to 18%, PtCo: 50% to 32%) after acid treatment, indicating the superior resistance of the ordered alloy structure towards M etching.

Detailed structural analysis of L1₀-Pt(M,Zn)@Pt NPs was conducted by HAADF-STEM and EDS mapping (Fig. 4, S7 and S8). Fig. 4A shows an HAADF-STEM image of a typical L1₀-Pt₅-Co_{2.5}Zn_{2.5} NP enclosed by major {111} and {001} facets and minor {110} facets. The NP consists of a thin Pt shell and intermetallic L1₀ core of alternating Pt and Co/Zn columns, represented by dots with brighter and darker contrast, respectively. Note that it is difficult to distinguish Zn from Co and Ni in the HAADF-STEM image because of their similar *Z* contrast. Fig. 4B presents the fast Fourier transform (FFT) image of Fig. 4A, which shows superlattice spots such as 001 and 1–10 characteristic of L1₀ structure. The interplanar spacing of {001} planes ($d\{001\}$) measured from the masked inverse FFT image was 0.372 nm (Fig. 4C and D), which agreed well with the lattice constant *c* of L1₀-Pt₅Co_{2.5}Zn_{2.5} NPs determined from XRD refinement. The L1₀ structure core was further verified by the elemental mapping images (Fig. 4E–I), which showed alternating layers of Pt and Co/Zn. The acid treatment of L1₀-Pt₅-Co_{2.5}Zn_{2.5} at 60 °C for 10 h provided a Pt-rich shell with a thickness of two to three atomic layers, as clearly seen in EDS line-scanning profiles (Fig. 4J and K), HAADF-STEM *Z*-contrast profiles (Fig. 4L and M), and electron energy loss spectroscopy mapping images (Fig. S21). XRD patterns before and after the acid treatment of representative L1₀-Pt₅Co_{2.5}Zn_{2.5}/C (Fig. S22) further confirmed the formation of core–shell structure. That is, no shift of the superlattice peaks was observed after acid treatment, indicating the L1₀ structure was robust. The small negative shift of the non-superlattice peaks was caused by the etching of M to form the shell structure.

To experimentally confirm the compressive strain in the Pt-rich shell, we measured the actual interatomic distances in the Pt-rich shell from the HAADF-STEM *Z*-contrast image in Fig. 4A (also see Fig. S23 and S24). The interatomic distance between neighboring atoms in the {001} planes projected from the <110> direction corresponds to $d\{110\}$. The average measured $d\{110\}$ values in the surface atomic layers were 0.266, 0.261, and 0.266 nm for the first, second, and third layer, respectively, which are considerably shorter than $d\{110\}$ of both pure Pt (0.277 nm), despite the Pt-rich composition, and the highly ordered alloy core (0.271 nm). A similar trend was observed for the {111} plane. These results strongly support that



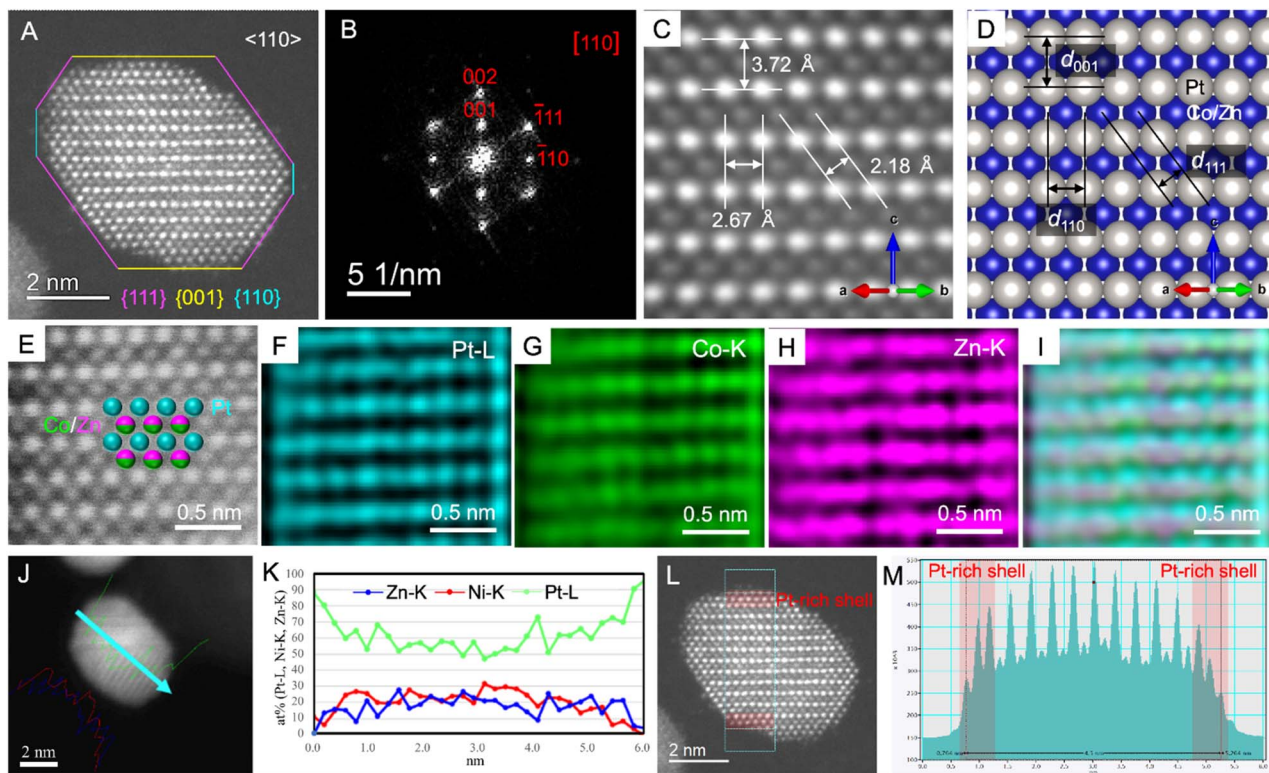


Fig. 4 Structural analyses of a single $L1_0$ - $Pt_5Co_{2.5}Zn_{2.5}@Pt$ NP. (A) HAADF-STEM image, (B) FFT image of (A) (zone axis is the $\langle 110 \rangle$ direction), (C) masked inverse FFT image of (B), and (D) schematic model of $L1_0$ -PtM along the $\langle 110 \rangle$ direction (Pt: gray, M: blue) corresponding to (C). (E–I) High-resolution STEM elemental mapping images after passing through a Wiener filter, (J) HAADF image, (K) EDS line-scan profiles showing the distributions of Pt, Ni, and Zn, (L) HAADF-STEM Z-contrast image, and (M) Z-contrast profile from the indicated area in (L).

the Pt-rich shells are subjected to compressive strain induced by the smaller lattice of the $L1_0$ -PtM core relative to that of the shell. However, because it is complicated to determine the average compressive surface strain of a sample macroscopically, the surface strain of Pt shells (see the Methods section in the SI for definition) was estimated by calculating the lattice mismatch between $L1_0$ -Pt(M,Zn) and pure Pt from the average lattice constant determined macroscopically by XRD measurements. The calculation results plotted in Fig. S3 showed that higher Zn content leads to lower surface strain. This is logical because the atomic radius of Zn (134 pm) is larger than those of Co (125 pm) and Ni (125 pm). However, the incorporation of low content of Zn can still lead to high δ and large compressive surface strain.

Overall, acid treatment provided NPs with $L1_0$ -Pt(M,Zn)@Pt core-shell structure by the effective etching of M/Zn components from the $L1_0$ -Pt(M,Zn) NP surface. The Pt shells showed compressive strain caused by the lattice mismatch between the Pt shells and $L1_0$ cores, which is promising for achieving simultaneous improvements of ORR durability and activity.

3.5 ORR electrocatalytic performance of highly ordered $L1_0$ -Pt(M,Zn)@Pt/C

The electrocatalytic performance of highly ordered $L1_0$ -Pt(M,Zn)@Pt/C in the acidic ORR was evaluated using a typical thin-film rotating disc electrode technique. Cyclic voltammetry (CV)

measurements were conducted in N_2 -saturated 0.1 M $HClO_4$ aqueous solution at room temperature until stable CV curves were obtained (Fig. 5A and D). ECSA of the samples was calculated from the charge of hydrogen underpotential deposition and normalized by the Pt loading mass (see the SI for details). The ECSA values of $L1_0$ -Pt(M,Zn)@Pt/C (40 – 60 m^2 g_{Pt}^{-1}) and commercial standard Pt/C (67 m^2 g_{Pt}^{-1}) tended to increase with decreasing NP size (Table S6). The surface areas of $L1_0$ -Pt(M,Zn)@Pt/C are much higher than those of recently reported PtM IMCs catalysts because of the smaller initial particle size with narrower distribution and their morphology retention without aggregation after low-temperature annealing.^{6,7,9,14}

After obtaining stable CV curves, linear sweep voltammetry (LSV) was used to study the ORR catalytic activity of the highly ordered catalysts. As examples, the LSV polarization curves measured in O_2 -saturated 0.1 M $HClO_4$ aqueous solution at 1600 rpm are shown in Fig. 5B and E. In both $L1_0$ -Pt(Co,Zn)@Pt and $L1_0$ -Pt(Ni,Zn)@Pt systems, the half-wave potential increased with the amount of Co or Ni. Specific activity (i_s) and mass activity (i_m) at 0.9 V vs. RHE were calculated from kinetically controlled current (i_k) and ECSA (Fig. 5C and F), where i_k was obtained from Koutecky–Levich plots of current extracted from LSVs measured at various rotation rates. The highest catalytic activity among the series of ternary $L1_0$ -Pt(M,Zn)@Pt/C was obtained for $L1_0$ - $Pt_5Co_4Zn_1@Pt/C$, which showed i_s of 1.71 mA cm_{Pt}^{-2} and i_m of 0.69 A mg_{Pt}^{-1} . These values are



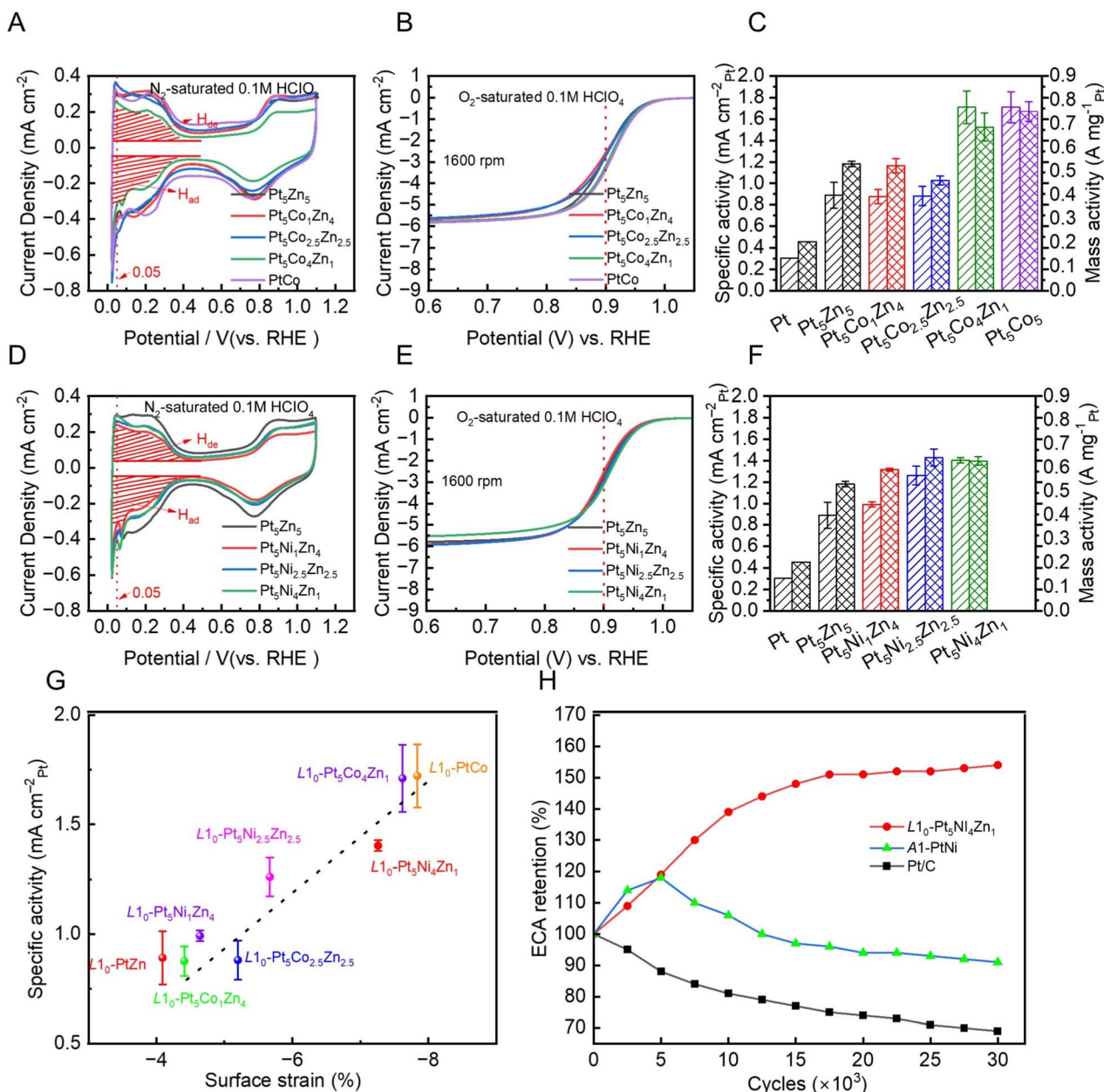


Fig. 5 Electrochemical catalytic activities of L10-Pt(M,Zn)@Pt/C. (A and D) CV curves, (B and E) ORR polarization curves at 1600 rpm, and (C and F) specific and mass activities at 0.9 V vs. SHE of highly ordered ($S > 0.7$) (A–C) L10-Pt(Co,Zn)@Pt/C and (D–F) L10-Pt(Ni,Zn)@Pt/C. (G) Correlation between specific activity and calculated surface strain of Pt shells. (H) ECSA retention of the catalysts during the ADT cycles in the RDE test.

comparable with those of binary L10-Pt₅Co₅@Pt/C and are approximately 5.6 and 3.3 times higher than those of commercial Pt/C, respectively.

To quantitatively discuss the effect of compressive strain in Pt-rich shells on ORR catalytic activity, the surface strain of each highly ordered sample with $S > 0.7$, which was estimated from the lattice mismatch of the ORR-active {111} facets shown in Fig. S3, was plotted against i_s (Fig. 5G). This plot showed the monotonic increase of i_s with compressive surface strain. Therefore, the high ORR activity of L10-Pt(M,Zn)@Pt/C likely results from the high compressive strain in the Pt-rich shell with a thickness of two to three atomic layers derived from the

smaller atomic radius of Co/Ni compared to that of Zn. The compressive strain induced in {111} planes is believed to modify the electronic structure, causing a downward shift of the d-band centre. This shift reduces the binding energy of oxygen intermediates and kinetically enhances ORR activity.^{34–37} In contrast, the poorly ordered L10-PtNi (~38%) exhibits a significantly lower ECSA (25 m² g_{Pt}⁻¹) and specific activity (0.491 mA cm_{Pt}⁻²) compared with the highly ordered L10-Pt(M,Zn) counterparts (Table S6). The inferior ORR performance of L10-PtNi can be primarily attributed to its low degree of ordering, which restricts the beneficial strain and structural effects associated with ordered intermetallic phases. These results suggest that



dealloying by M leaching and coarsening by agglomeration and Ostwald ripening of NPs during electrochemical cleaning processes prior to activity evaluation decrease activity and ECSA;³⁸ that is, the high *S* of L1₀-Pt(M,Zn)@Pt/C contributes the improvement of both catalytic activity and durability.

To further confirm the exceptional durability of the highly ordered L1₀-Pt(M,Zn)@Pt/C, accelerated durability tests (ADTs) were performed on Pt/C, A1-PtNi@Pt/C, and the representative L1₀-Pt₅Ni₄Zn₁@Pt/C in a half-cell configuration for comparison. The ECSA retention as a function of cycle number revealed a continuous decline for commercial Pt/C, retaining only ~69% after 30 000 cycles (Fig. 5H). In contrast, both L1₀-Pt₅Ni₄Zn₁@Pt/C and disordered A1-PtNi@Pt/C exhibited an initial increase in ECSA during the early stages of ADT. This phenomenon is generally attributed to electrochemical surface activation, including selective dissolution of less noble metals and surface reconstruction, which exposes previously inaccessible Pt active sites.^{39–41} With continued cycling, the disordered A1-PtNi@Pt/C catalyst experienced rapid ECSA decay following the initial activation, indicative of accelerated Ni leaching and structural degradation. Conversely, the highly ordered L1₀-Pt₅-Ni₄Zn₁@Pt/C maintained a sustained increase in ECSA throughout the ADT, suggesting that atomic ordering effectively suppresses excessive metal dissolution while enabling controlled surface activation. These findings are corroborated by TEM images before and after ADT (Fig. S26), which revealed significant particle growth for Pt/C and A1-PtNi@Pt/C, whereas the particle size of L1₀-Pt₅Ni₄Zn₁@Pt/C remained essentially unchanged. These observations underscore the superior structural stability of the ordered intermetallic catalyst under prolonged cycling conditions.

4. Conclusions

A feasible strategy to synthesize highly ordered IMC NPs with well-defined structures and compositions was developed. The ordering degree of L1₀-PtM NPs was increased and aggregation was prevented by Zn incorporation at low temperature. The ordering degree was greatly improved while maintaining a strain effect by decreasing the amount of Zn, which gave high ORR specific activity under harsh electrochemical conditions. In particular, L1₀-Pt₅Co₄Zn₁ showed a mass activity of 0.69 A mg_{Pt}⁻¹ and specific activity of 1.71 mA cm_{Pt}⁻², demonstrating its potential for fuel-cell applications. By precisely controlling NP composition, a comprehensive map of the correlation between the strain effect and ORR activity was constructed, which showed that specific activity increases monotonically with the compressive strain of surface Pt. These results provide us with insight into the tuning of ORR catalytic activity by finely controlling the structures of IMC NPs.

Author contributions

W. T., R. S., T. T. conceived the study. W. T., R. S. designed the synthesis scheme. W. T. performed the synthesis. W. T., R. S., K. M. were responsible for the characterization. W. T., R. S., T. U., Y. U. measured the electrochemical catalytic properties. W.

T., R. S. collected and analyzed the HAADF-STEM images and EDX elemental maps. Y. T. performed theoretical calculations. W. T., R. S., T. T. co-wrote the manuscript. All authors discussed the results and commented on the manuscript.

Conflicts of interest

There are no conflicts to declare.

Data availability

The data supporting this article have been included as part of the supplementary information (SI). Supplementary information: SI figures (Fig. S1–S26) and tables (Tables S1–S7) (PDF). See DOI: <https://doi.org/10.1039/d5ta08256k>.

Acknowledgements

The PEMFC project commissioned by the New Energy and Industrial Technology Development Organization (NEDO) (Grant No. 20001199-0 [T. T.]). Japan Science and Technology Agency, Core Research for Evolutionary Science and Technology (JST-CREST) (Grant No. JPMJCR21B4 [T. T.]). The Japan Society for the Promotion of Science (JSPS) KAKENHI for Scientific Research (S) (Grant No. JP24H00053 [T. T.]) and Scientific Research (B) (Grant No. JP23K26627 [R. S.]). High-resolution STEM analyses were performed under the NEDO FC-Platform. We thank Natasha Lundin, PhD, from Edanz (<https://jp.edanz.com/ac>) for editing a draft of this manuscript.

References

- 1 R. Borup, J. Meyers, B. Pivovar, Y. S. Kim, R. Mukundan, N. Garland, D. Myers, M. Wilson, F. Garzon, D. Wood, P. Zelenay, K. More, K. Stroh, T. Zawodzinski, J. Boncella, J. E. McGrath, M. Inaba, K. Miyatake, M. Hori, K. Ota, Z. Ogumi, S. Miyata, A. Nishikata, Z. Siroma, Y. Uchimoto, K. Yasuda, K.-i. Kimijima and N. Iwashita, *Chem. Rev.*, 2007, **107**, 3904–3951.
- 2 J. K. Nørskov, J. Rossmeisl, A. Logadottir, L. Lindqvist, J. R. Kitchin, T. Bligaard and H. Jónsson, *J. Phys. Chem. B*, 2004, **108**, 17886–17892.
- 3 C. Chen, Y. Kang, Z. Huo, Z. Zhu, W. Huang, H. L. Xin, J. D. Snyder, D. Li, J. A. Herron, M. Mavrikakis, M. Chi, K. L. More, Y. Li, N. M. Markovic, G. A. Somorjai, P. Yang and V. R. Stamenkovic, *Science*, 2014, **343**, 1339–1343.
- 4 X. Tian, X. Zhao, Y.-Q. Su, L. Wang, H. Wang, D. Dang, B. Chi, H. Liu, E. J. M. Hensen, X. W. Lou and B. Y. Xia, *Science*, 2019, **366**, 850–856.
- 5 D. Wang, H. L. Xin, R. Hovden, H. Wang, Y. Yu, D. A. Muller, F. J. DiSalvo and H. D. Abruña, *Nat. Mater.*, 2013, **12**, 81–87.
- 6 J. Li, S. Sharma, X. Liu, Y.-T. Pan, J. S. Spendelow, M. Chi, Y. Jia, P. Zhang, D. A. Cullen, Z. Xi, H. Lin, Z. Yin, B. Shen, M. Muzzio, C. Yu, Y. S. Kim, A. A. Peterson, K. L. More, H. Zhu and S. Sun, *Joule*, 2019, **3**, 124–135.



- 7 J. Li, Z. Xi, Y. T. Pan, J. S. Spendelow, P. N. Duchesne, D. Su, Q. Li, C. Yu, Z. Yin, B. Shen, Y. S. Kim, P. Zhang and S. Sun, *J. Am. Chem. Soc.*, 2018, **140**, 2926–2932.
- 8 J. Liang, Z. Zhao, N. Li, X. Wang, S. Li, X. Liu, T. Wang, G. Lu, D. Wang, B.-J. Hwang, Y. Huang, D. Su and Q. Li, *Adv. Energy Mater.*, 2020, **10**, 2000179.
- 9 W. J. Zeng, C. Wang, Q. Q. Yan, P. Yin, L. Tong and H. W. Liang, *Nat. Commun.*, 2022, **13**, 7654.
- 10 T.-W. Song, C. Xu, Z.-T. Sheng, H.-K. Yan, L. Tong, J. Liu, W.-J. Zeng, L.-J. Zuo, P. Yin, M. Zuo, S.-Q. Chu, P. Chen and H.-W. Liang, *Nat. Commun.*, 2022, **13**, 6521.
- 11 C.-L. Yang, L.-N. Wang, P. Yin, J. Liu, M.-X. Chen, Q.-Q. Yan, Z.-S. Wang, S.-L. Xu, S.-Q. Chu, C. Cui, H. Ju, J. Zhu, Y. Lin, J. Shui and H.-W. Liang, *Science*, 2021, **374**, 459–464.
- 12 J. Liang, N. Li, Z. Zhao, L. Ma, X. Wang, S. Li, X. Liu, T. Wang, Y. Du, G. Lu, J. Han, Y. Huang, D. Su and Q. Li, *Angew. Chem., Int. Ed.*, 2019, **58**, 15471–15477.
- 13 J. Li, S. Sharma, K. Wei, Z. Chen, D. Morris, H. Lin, C. Zeng, M. Chi, Z. Yin, M. Muzzio, M. Shen, P. Zhang, A. A. Peterson and S. Sun, *J. Am. Chem. Soc.*, 2020, **142**, 19209–19216.
- 14 T. Wang, J. Liang, Z. Zhao, S. Li, G. Lu, Z. Xia, C. Wang, J. Luo, J. Han, C. Ma, Y. Huang and Q. Li, *Adv. Energy Mater.*, 2019, **9**, 1803771.
- 15 Y. Yan, J. S. Du, K. D. Gilroy, D. Yang, Y. Xia and H. Zhang, *Adv. Mater.*, 2017, **29**, 1605997.
- 16 J. Liang, Y. Wan, H. Lv, X. Liu, F. Lv, S. Li, J. Xu, Z. Deng, J. Liu, S. Zhang, Y. Sun, M. Luo, G. Lu, J. Han, G. Wang, Y. Huang, S. Guo and Q. Li, *Nat. Mater.*, 2024, **23**, 1259–1267.
- 17 R.-Y. Shao, X.-C. Xu, Z.-H. Zhou, W.-J. Zeng, T.-W. Song, P. Yin, A. Li, C.-S. Ma, L. Tong, Y. Kong and H.-W. Liang, *Nat. Commun.*, 2023, **14**, 5896.
- 18 Z. Chen, J. Liu, B. Yang, M. Lin, C. Molochas, P. Tsiakaras and P. Shen, *J. Colloid Interface Sci.*, 2023, **652**, 388–404.
- 19 Y. Yu, W. Yang, X. Sun, W. Zhu, X. Z. Li, D. J. Sellmyer and S. Sun, *Nano Lett.*, 2014, **14**, 2778–2782.
- 20 A. Cebollada, D. Weller, J. Sticht, G. R. Harp, R. F. C. Farrow, R. F. Marks, R. Savoy and J. C. Scott, *Phys. Rev. B: Condens. Matter Mater. Phys.*, 1994, **50**, 3419–3422.
- 21 T. Degen, M. Sadki, E. Bron, U. König and G. Nénert, *Powder Diffr.*, 2014, **29**, S13–S18.
- 22 T. Ozaki, *Phys. Rev. B: Condens. Matter Mater. Phys.*, 2003, **67**, 155108.
- 23 A. van de Walle, P. Tiwary, M. de Jong, D. L. Olmsted, M. Asta, A. Dick, D. Shin, Y. Wang, L. Q. Chen and Z. K. Liu, *Calphad*, 2013, **42**, 13–18.
- 24 S. Takamoto, C. Shinagawa, D. Motoki, K. Nakago, W. Li, I. Kurata, T. Watanabe, Y. Yayama, H. Iriguchi, Y. Asano, T. Onodera, T. Ishii, T. Kudo, H. Ono, R. Sawada, R. Ishitani, M. Ong, T. Yamaguchi, T. Kataoka, A. Hayashi, N. Charoenphakdee and T. Ibuka, *Nat. Commun.*, 2022, **13**, 2991.
- 25 C. Huang, H. Liu, Y. Tang, Q. Lu, S. Chu, X. Liu, B. Shan and R. Chen, *Appl. Catal., B*, 2023, **320**, 121986.
- 26 A. Miura, H. Wang, B. M. Leonard, H. D. Abruña and F. J. DiSalvo, *Chem. Mater.*, 2009, **21**, 2661–2667.
- 27 S. Mourdikoudis and L. M. Liz-Marzán, *Chem. Mater.*, 2013, **25**, 1465–1476.
- 28 G. Feng, F. Ning, Y. Pan, T. Chen, J. Song, Y. Wang, R. Zou, D. Su and D. Xia, *J. Am. Chem. Soc.*, 2023, **145**, 11140–11150.
- 29 Z. Cui, H. Chen, M. Zhao and F. J. DiSalvo, *Nano Lett.*, 2016, **16**, 2560–2566.
- 30 K. Takanashi, S. Mitani, M. Sano, H. Fujimori, H. Nakajima and A. Osawa, *Appl. Phys. Lett.*, 1995, **67**, 1016–1018.
- 31 S. Sun, C. B. Murray, D. Weller, L. Folks and A. Moser, *Science*, 2000, **287**, 1989–1992.
- 32 G. Kim, T. Hiratsuka, H. Naganuma, M. Oogane and Y. Ando, *J. Phys.: Conf. Ser.*, 2010, **200**, 052011.
- 33 R. A. Ristau, K. Barmak, L. H. Lewis, K. R. Coffey and J. K. Howard, *J. Appl. Phys.*, 1999, **86**, 4527–4533.
- 34 A. Kulkarni, S. Siahrostami, A. Patel and J. K. Nørskov, *Chem. Rev.*, 2018, **118**, 2302–2312.
- 35 Z. Wang, Y. Mai, Y. Yang, L. Shen and C. Yan, *ACS Appl. Mater. Interfaces*, 2021, **13**, 38138–38146.
- 36 Z. Wang, Y. Yang, X. Wang, Z. Lu, C. Guo, Y. Shi, H. Tan, L. Shen, S. Cao and C. Yan, *J. Mater. Chem. A*, 2022, **10**, 12141–12149.
- 37 Y. Zhou, Z. Zhou, R. Shen, R. Ma, Q. Liu, G. Cao and J. Wang, *Energy Storage Mater.*, 2018, **13**, 189–198.
- 38 X. Xie, A. L. M. Sandhya, L. Piliari, M. Vorokhta, I. Motolínová and I. Khalakhan, *Appl. Catal., B*, 2023, **325**, 122328.
- 39 C. Lim, A. R. Fairhurst, B. J. Ransom, D. Haering and V. R. Stamenkovic, *ACS Catal.*, 2023, **13**, 14874–14893.
- 40 M. Gatalo, A. M. Bonastre, L. J. Moriau, H. Burdett, F. Ruiz-Zepeda, E. Hughes, A. Hodgkinson, M. Šála, L. Pavko, M. Bele, N. Hodnik, J. Sharman and M. Gaberšček, *ACS Appl. Energy Mater.*, 2022, **5**, 8862–8877.
- 41 X. Tong, J. Zhang, G. Zhang, Q. Wei, R. Chenitz, J. P. Claverie and S. Sun, *Chem. Mater.*, 2017, **29**, 9579–9587.

